

Supramolecular dye polymers for aggregation-induced photocatalysis

Received: 20 September 2025

Accepted: 13 April 2026

Published online: 18 May 2026

Check for updates

Marianna Barbieri¹, David Cappelletti¹, Luca Vaccarin¹, Marco Villa², Luca Catalano³, Khai-Nghi Truong⁴, Fabrizio Nestola⁵, Elisa Pelorosso¹, Alessandro Aliprandi¹, Andrea Sartorel¹, Paola Ceroni², Francesca Arcudi¹ & Luka Đorđević¹✉

Aggregation can profoundly alter the excited-state properties of organic chromophores; however, crystalline supramolecular polymers are often targeted for photocatalytic conversion of solar energy due to favourable charge delocalization or exciton transport. Here we exploit aggregation as a strategy for organic chromophore rigidification to activate photocatalysis by stabilizing localized excited states. Using amphiphilic distyrylanthracene derivatives, we show that aggregation in water enhances the availability of excited states, enabling light-driven transformations of solar energy into storable fuels. We found enhanced reactivity to correlate with increased local excited-state population, underlining the role of self-assembly in restricting intramolecular motion and suppressing unproductive non-radiative decay. We observed photocatalysis to be maximized in kinetically trapped aggregates, outperforming their thermodynamic counterparts, to challenge conventional paradigm that favourable activities require extended assemblies. By achieving excited-state confinement and reactivity instead of charge delocalization, this work reports aggregation-induced photocatalysis as a strategy for preparing photostable, emissive and functional organic photocatalysts in water.

The direct conversion of sunlight into chemical energy by organic molecular materials remains a central objective in artificial photosynthesis^{1–5}. Organic molecules are versatile photocatalysts because they offer structural tunability, high extinction coefficients and rational molecular engineering. They have traditionally been utilized either as molecular dyes in homogeneous solution^{6–9} or as semiconductors in heterogeneous systems^{10–13}. Although molecular systems offer defined excited-state redox potentials and facile processing, their use is often limited by poor photostability and low photocatalytic efficiencies. Conversely, organic semiconductors benefit from delocalized charge transport and robustness but often sacrifice molecular precision and processability.

A major challenge in leveraging organic dyes for light-driven catalysis is the loss of reactivity upon aggregation. In many cases,

chromophore–chromophore interactions can quench excited states through trap states, excimer formation, intermolecular charge or electron transfer, intersystem crossing and H-aggregate formation^{14,15}. As a result, the excited states are typically deactivated quickly in the aggregated state. Strategies to overcome this and exploit molecules in photocatalysis include preparation of metallacages¹⁶, macrocycles¹⁷, using surfactants¹⁸, formation of inclusion complexes¹⁹ and co-assembling dyes with insulating (macro)molecules^{20–23}.

Although aggregation is often detrimental to photocatalysis, it can also be beneficial for some organic dyes^{12,24–27}. Inspired by biological photosystems, supramolecular assemblies have been used to enhance photocatalysis through exciton delocalization and long-range charge separation. In these systems, aggregation extends excited

¹Department of Chemical Sciences, University of Padova, Padova, Italy. ²Department of Chemistry ‘Giacomo Ciamician’, Alma Mater Studiorum–University of Bologna, Bologna, Italy. ³Department of Life Sciences, University of Modena and Reggio Emilia, Modena, Italy. ⁴Rigaku Europe SE, Neu-Isenburg, Germany. ⁵Department of Geosciences, University of Padova, Padova, Italy. ✉e-mail: luka.dordevic@unipd.it

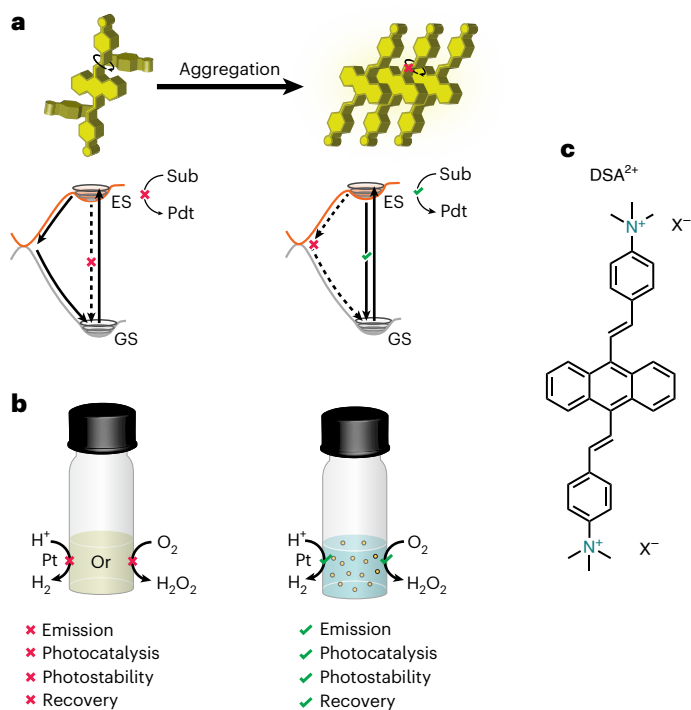


Fig. 1 | AIP with the DSA²⁺ supramolecular dye polymers. **a**, Overview of the rigidification in DSA²⁺ amphiphiles through supramolecular polymerization, obstructing otherwise rapid non-radiative decay of the photoexcited state. **b**, Aggregation leads to excited-states enhancement and photocatalysis (H₂ or H₂O₂ photoproduction), with improved dye properties such as stability and recovery. **c**, Chemical structure of distyrylanthracene (DSA²⁺) amphiphile, where X⁻ indicates the counteranion. GS, ground state; ES, excited state; Sub, substrate; Pdt, product.

states across planar or rigid chromophores through π - π stacking or donor-acceptor interactions in crystalline assemblies^{1–5,28–35}. In these systems, aggregation-caused emission quenching can enable exciton migration and charge separation across crystalline domains, thereby allowing organic nanostructures to drive reactions such as H₂ evolution and H₂O₂ production. However, this strategy depends on strong electronic coupling between chromophores and thus often requires planar scaffolds and specific packing motifs that are difficult to predict and design rationally.

Here, we report aggregation-induced photocatalysis (AIP), a mechanism for organic dye photocatalysis that does not rely on solubilized chromophores or exciton-delocalized assemblies. Instead, molecular packing restricts intramolecular motion and increases the population of reactive excited states (Fig. 1a,b), paralleling the rigidification mechanism of aggregation-induced emission (AIE)^{36–43}. Using an amphiphilic distyrylanthracene dye (DSA²⁺, Fig. 1c), we show that aggregation can be tuned by concentration, counterion identity or salt addition to form nanocrystals in water that drive photocatalytic H₂ and H₂O₂ production with enhanced photostability. In contrast to self-assembled photocatalysts that rely on charge delocalization, these materials operate through localized excited states enabled by rigidification. The photocatalytic performance further depends on the aggregation pathway and extends to a structurally unrelated fluorophore scaffold.

Results and discussion

Photophysical and morphological properties of dye aggregates

The DSA²⁺ amphiphile has a distyrylanthracene core bearing two trimethylammonium groups (Fig. 1c). It was synthesized as diiodide salt (DSAI), and counterion exchange reactions afforded DSAX

compounds as chloride (DSACl), bromide (DSABr), nitrate (DSANO₃) and hexafluorophosphate (DSAPF₆) salts (Supplementary Information section 3). The molecules were characterized by ¹H and ¹³C nuclear magnetic resonance spectroscopies, mass spectrometry, ultraviolet (UV)-visible absorption spectroscopy and infrared spectroscopy (Supplementary Figs. 1–32).

We first measured the absolute fluorescence quantum yields (Φ_{FL}) of DSAX salts in water (0–1.5 mM) to monitor the aggregation, as Φ_{FL} is a sensitive reporter of restricted intramolecular rotation in the aggregate state and thus of AIE^{44,45}. DSAX samples with hydrated counteranions, such as Cl⁻, Br⁻ and NO₃⁻, showed no aggregation, as indicated by low fluorescence ($\Phi_{\text{FL}} \leq 1.1\%$), whereas hydrophobic PF₆⁻ caused the molecules to be always aggregated, as evidenced by relative high $\Phi_{\text{FL}} \approx 6.9\%$ in these suspensions (Fig. 2a and Supplementary Figs. 33 and 34). Among the DSAX salts, only the iodide form (DSAI) exhibited concentration-dependent aggregation and emission behaviour, from weakly emissive dilute solutions to progressively fluorescent yellow suspensions at higher concentrations (Fig. 2a and Supplementary Figs. 35–38). This mirrors previous observations that higher concentrations of amphiphilic monomers provide self-screening for repulsive electrostatic interactions⁴⁶. The specific ion effect is opposite to the conventional Hofmeister series in which charge-dense ions (for example, Cl⁻, Br⁻ and NO₃⁻) promote aggregation of macromolecules by reducing solubility^{47,48}. Here, instead, charge-diffuse ions (I⁻ and PF₆⁻) promote aggregation, consistent with a reverse Hofmeister effect driven by ion pairing and monomers stacking.

We further investigated the polymerization behaviour of DSAI, which can exist as either dissolved monomers or aggregates depending on concentration. Organic solvent minimizes interactions between monomers and promotes disaggregation through dissolution, whereas salts and electrolytes enhance charge screening and thus promote supramolecular polymerization. Hence, plotting Φ_{FL} as a function of [DSAI] and either fraction of organic solvent (f_{DMSO} , as vol% with water) or [NaI] provide assembly landscapes that visualize the propensity of DSAI to self-assemble under different conditions (Fig. 2b,c and Supplementary Figs. 40–43). In both cases, aggregation is promoted either by increasing the water content, which strengthens hydrophobic interactions or by increasing [NaI], which screens the positive charges, reduces electrostatic repulsion and promotes hydrophobic collapse. Consistent with this mechanism, aggregation of DSAX (X = Cl⁻, Br⁻, NO₃⁻ and I⁻) can be induced by addition of the corresponding sodium salts (NaX), which increase charge screening and promote aggregate formation (Supplementary Figs. 44–46). Aggregation can also be triggered by salts bearing counteranions different from those originally paired with the dye; for example, NaI induces aggregation of DSACl (Supplementary Figs. 47 and 48), showing that both ionic strength and counteranion identity contribute. Supporting this interpretation, counteranions are not merely dissociated but are embedded within the nanostructures (Supplementary Figs. 48–54).

We next characterized the nanostructures formed upon DSAI self-assembly using complementary techniques from the nanoscale to the bulk. Transmission electron microscopy revealed flat, elongated nanoribbons with high aspect ratio (Fig. 2d and Supplementary Fig. 55), indicating a preferential growth direction, probably via hydrophobic collapse of the aromatic cores. Atomic force microscopy showed that these flat nanoribbons are stacked lamellar structures with discrete step heights of ~2 nm (Fig. 2e,f and Supplementary Fig. 56). X-ray diffraction on the bulk powder revealed the high degree of crystallinity of the nanoribbons (Supplementary Fig. 57). Although bulk single crystals of pure DSAI suitable for X-ray analysis could not be obtained in water, continuous three-dimensional electron diffraction (3D-ED)^{49,50} provided atomically precise structural characterization of the nanocrystalline aggregates. 3D-ED analysis revealed face-on molecular packing in the aggregates (Fig. 2g and Supplementary Figs. 58–60), in which the

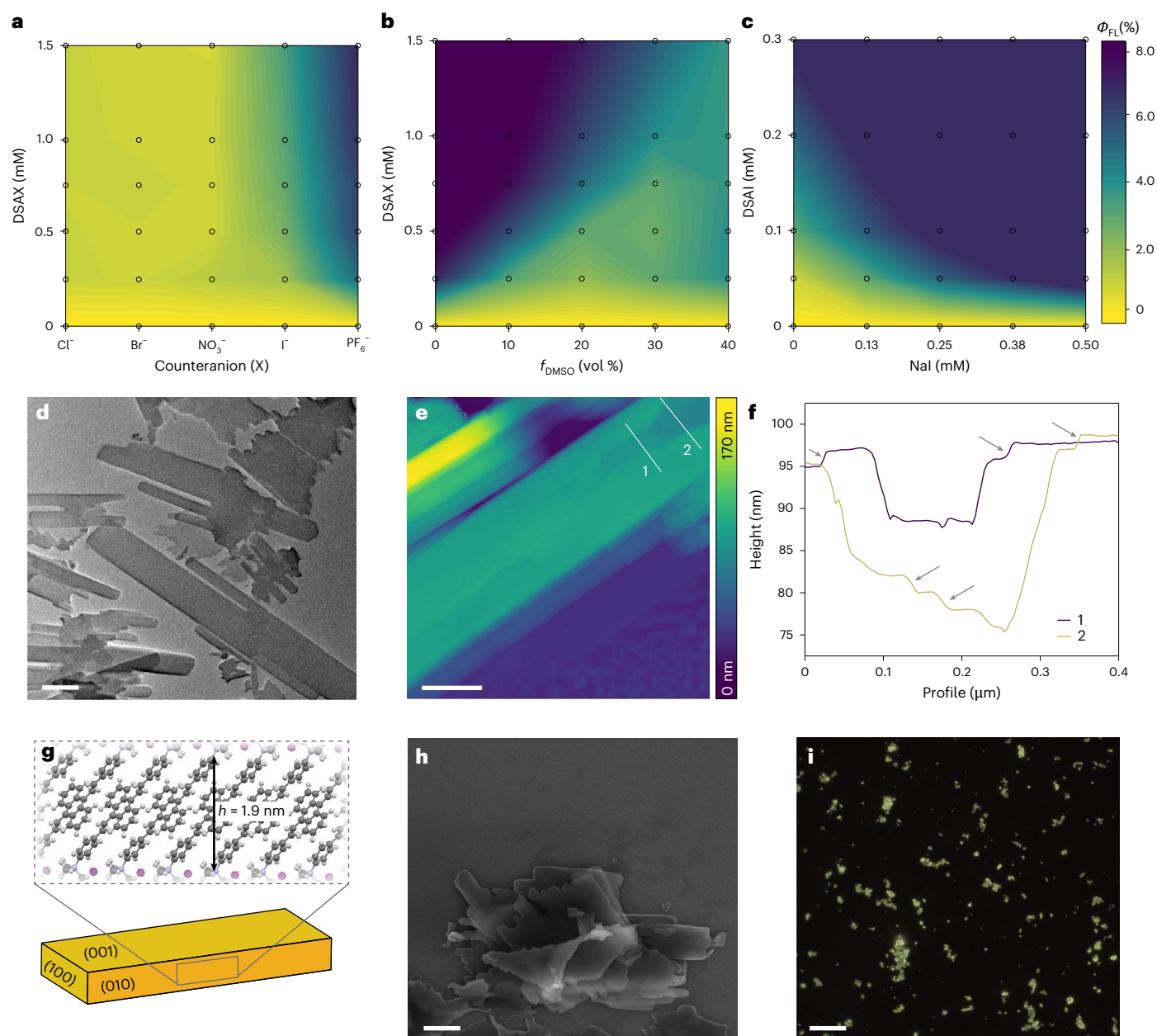


Fig. 2 | Supramolecular polymerization of DSA²⁺ amphiphiles into fluorescent and crystalline nanostructures. **a**, Assembly landscapes at different concentrations of DSA²⁺ amphiphile (mM) with selected counteranions (Cl⁻, Br⁻, NO₃⁻, I⁻ and PF₆⁻). **b**, Assembly landscape at different concentrations of DSAI amphiphile (mM) under various ratios between water and organic solvent (DMSO). **c**, Assembly landscape at different concentrations of DSAI amphiphile (mM) with different amount of salt (NaI, mM). **d**, Transmission electron microscope (TEM) image of DSAI supramolecular nanostructures in water (DSAI 0.05 mM, NaI 0.5 mM). Scale bar, 500 nm. **e**, Atomic force microscope image of drop-casted aqueous suspension of DSAI supramolecular

nanostructures (DSAI 0.05 mM, NaI 0.5 mM). Scale bar, 400 nm. **f**, Height profiles by AFM of selected sections (indicated by 1 and 2 from **e**) and relative step heights of ~2 nm (grey arrows). **g**, A schematic representation of the dominant crystallographic faces of a DSAI nanocrystal, with a zoom-in on the layered slipped π - π stacking viewed along the b axis, as determined from 3D-ED data (atoms shown as ball and stick). **h**, Scanning electron microscope image of DSAI supramolecular nanostructures in water (DSAI 0.05 mM, NaI 0.5 mM). Scale bar, 400 nm. **i**, WFM image of DSAI supramolecular nanostructures in water (DSAI 0.05 mM, NaI 0.5 mM). Scale bar, 20 μ m.

DSAI chromophores adopt a typical slipped π - π stacked arrangement ($\theta_{\text{slip}} \approx 44.6^\circ$, centre-to-centre distance of -5.7 \AA) with an interlayer spacing of -1.9 nm typical for crystalline aromatic systems such as acenes and related polycyclic π -conjugated molecules. Scanning electron microscopy (SEM) showed that these nanoribbons assemble both laterally and through inter-ribbon stacking into micron-sized crystalline platelets (Fig. 2h and Supplementary Fig. 61), whereas widefield fluorescence microscopy (WFM) revealed bright emissive micron-sized domains (Fig. 2i and Supplementary Fig. 62).

Supramolecular aggregation can be systematically controlled by counterion, solvent environment and charge screening to yield structurally ordered, emissive nanoribbons, establishing the structural basis for the photocatalytic studies that follow.

Aggregation-induced light-driven ROS and H₂O₂ generation
We next investigated whether supramolecular assembly of DSA²⁺ improves light-driven generation of reactive oxygen species (ROS), modulating aggregation through counterion exchange, chromophore

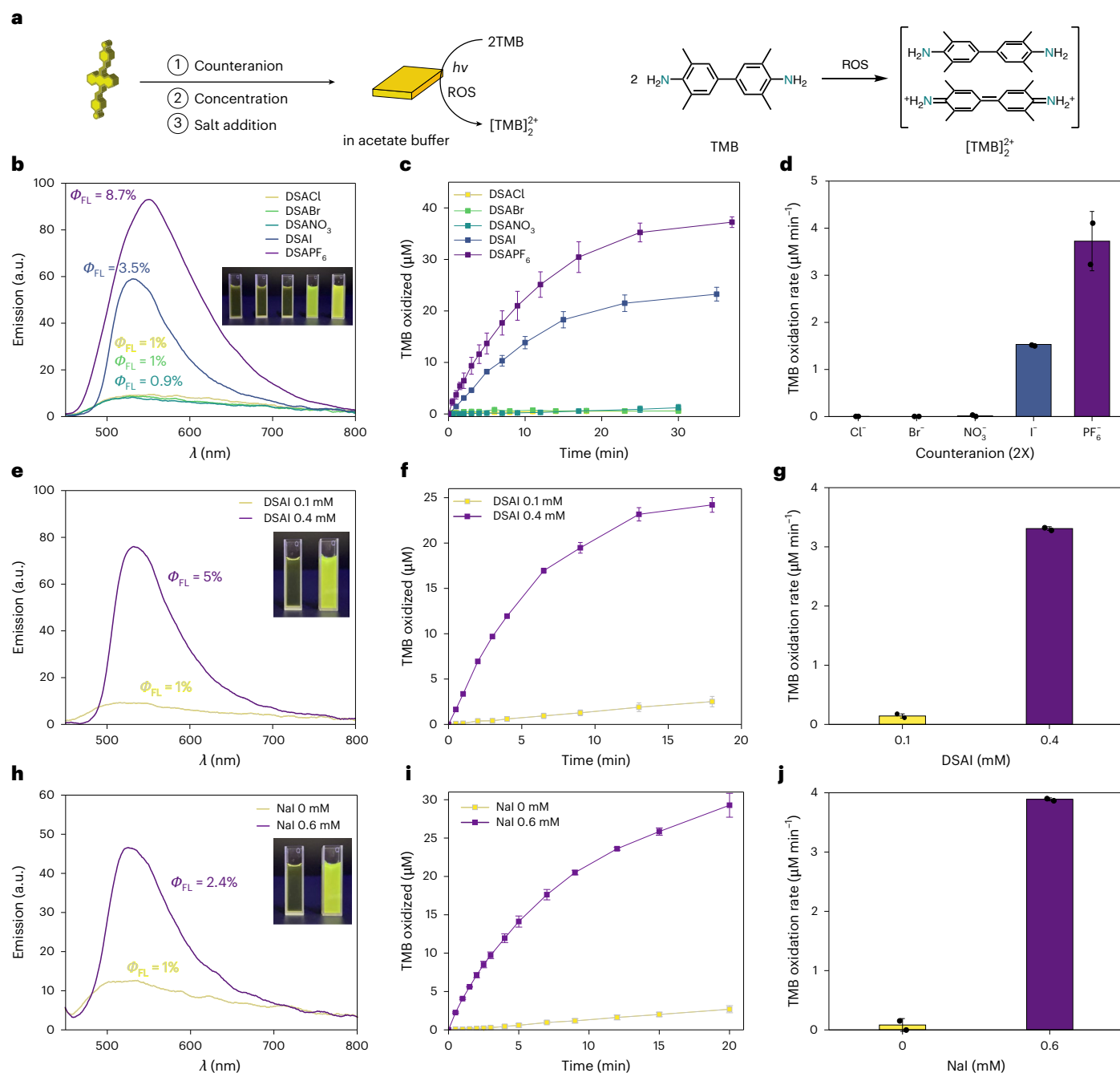


Fig. 3 | Light-driven ROS generation by DSA²⁺ nanostructures. **a**, A schematic representation of aggregation modes (counteranion used, concentration and ionic strength) to obtain fluorescent nanostructures that mediate oxidation of the TMB probe into a blue charge-transfer complex (white-light LED, 180 mW cm⁻² under air). **b**, Fluorescence emission spectra and fluorescence quantum yields (Φ_{FL}) of DSAX (0.3 mM) with different counteranions (X = Cl⁻, Br⁻, NO₃⁻, I⁻ and PF₆⁻). The inset shows the DSAX samples under UV light (from left to right: Cl⁻, Br⁻, NO₃⁻, I⁻ and PF₆⁻). **c**, Light-driven TMB (134 μ M) oxidation by DSAX over time. Statistics are from two independent groups. **d**, TMB oxidation rate (0.0 ± 0.0 , 0.0 ± 0.0 , 0.01 ± 0.02 , 1.5 ± 0 and 3.7 ± 0.6 μ M min⁻¹) extracted from traces in **c**. Statistics are from two independent groups. **e**, Fluorescence emission spectra and fluorescence quantum yields (Φ_{FL}) of DSAI at 0.1 mM concentration

(yellow trace) and 0.4 mM (purple trace). The inset shows DSAI 0.1 mM (left) and 0.4 mM (right) samples under UV light. **f**, Light-driven TMB (134 μ M) oxidation by DSAI over time. Statistics are from two independent groups. **g**, TMB oxidation rate (0.14 ± 0.04 and 3.3 ± 0 μ M min⁻¹) extracted from traces in **f**. Statistics are from two independent groups. **h**, Fluorescence emission spectra and fluorescence quantum yield (Φ_{FL}) of DSAI (0.1 mM) without (yellow trace, 0.0 mM NaI) and with presence of salt (purple trace, 0.6 mM NaI). The inset shows DSAI 0.1 mM samples without (left) and with NaI present (right) under UV light. **i**, Light-driven TMB (134 μ M) oxidation by DSAI without and with presence of NaI over time. Statistics are from two independent groups. **j**, TMB oxidation rate (0.08 ± 0.11 and 3.9 ± 0 μ M min⁻¹) extracted from traces in **i**. Statistics are from two independent groups.

concentration and ionic strength (Fig. 3a). In each case, we assessed both fluorescence quantum yield (Φ_{FL}) and light-driven ROS generation, the latter using the 3,3',5,5'-tetramethylbenzidine (TMB)^{51,52} probe, which is oxidized by ROS to form a blue-coloured charge-transfer complex (Fig. 3a).

Under the buffer conditions used for the light-driven TMB oxidation (acetate buffer, 0.1 M, pH 5), hydrophobic and poorly hydrated anions, particularly I⁻ and PF₆⁻, increased Φ_{FL} from $\leq 1.1\%$ (for Cl⁻, Br⁻ and NO₃⁻ salts) to 3.5% and 8.7% for DSAI and DSAPF₆, respectively (Fig. 3b). This fluorescence enhancement strongly correlates with

photocatalytic activity under white-light irradiation: DSAPF₆ exhibited the highest rate of TMB oxidation ($\nu_0 = 3.7 \mu\text{M min}^{-1}$), followed by I⁻ ($\nu_0 = 1.5 \mu\text{M min}^{-1}$), whereas Cl⁻, Br⁻ and NO₃⁻ showed no or minimal activity (Fig. 3c,d and Supplementary Fig. 63). This specific ion effect trend follows a reverse Hofmeister effect already observed in unbuffered water, suggesting that charge-diffuse anions reduce solvation and enable greater excited-states utilization in photocatalysis. Increasing DSAI from 0.1 mM to 0.4 mM in acetate buffer increased Φ_{FL} about fivefold, from 1.1% to 4.8% (Fig. 3e), consistent with AIE. Correspondingly, the rate of TMB oxidation increases by more than one order of magnitude, from $\nu_0 = 0.14 \mu\text{M min}^{-1}$ to $\nu_0 = 3.3 \mu\text{M min}^{-1}$ (Fig. 3f,g and Supplementary Fig. 64), confirming that concentration-driven self-assembly translates into enhanced ROS generation. Salt-induced aggregation was probed by adding NaI to a dilute DSAI solution in acetate buffer. Even at constant chromophore concentration (0.1 mM), the presence of NaI (0.6 mM) increased Φ_{FL} from 1.1% to 2.4% (Fig. 3h) and the ROS production rate from $\nu_0 = 0.08 \mu\text{M min}^{-1}$ to $\nu_0 = 3.9 \mu\text{M min}^{-1}$ (Fig. 3i,j and Supplementary Fig. 65). These results highlight the role of electrostatic screening in driving aggregation and suggest that subtle environmental changes can modulate functional output via supramolecular polymerization.

To assess how supramolecular aggregation affects the excited states, we measured fluorescence lifetimes (τ_{avg}) of solution and aggregates by time-correlated single photon counting. In all cases, the nanosecond fluorescence decays (Supplementary Figs. 66–70) indicate singlet excited states and motivated further femtosecond and nanosecond transient absorption measurements (TAS). In solution, the monomeric chromophore displayed a transient band at 620 nm that shifted to 545 nm and then decayed with lifetimes of 17 and 79 ps, respectively, consistent with rapid styryl photoisomerization in DSAI (Supplementary Fig. 71) and reported femtosecond transient absorption measurements spectra of 9,10-distyrylanthracene derivatives⁵³. By contrast, DSAI aggregates showed no shift of the excited-state absorption bands (Supplementary Fig. 72). Kinetic analysis identified a fast 21-ps component, similar to the monomer, and a slower 320-ps component, as expected for rigidification-induced suppression of photoisomerization decay and enhanced excited-state stabilization. At 7 ns, the excited-state absorption band at 539 nm was still present, consistent with the lowest triplet excited state; this was confirmed by ns-TAS (Supplementary Fig. 73), although no phosphorescence was observed in the solid state at 77 K (Supplementary Fig. 74). The emission and transient absorption spectra of the aggregates also resemble those of the monomer in rigid media⁵³ (Supplementary Fig. 75), supporting the formation of localized singlet and triplet excited states in the aggregated state. These results show that aggregation enhances photocatalysis by increasing the population of localized excited states. Although weak coupling interactions in slip-stacked molecules cannot be excluded, the large π - π stacking distances (> 5 Å), the absence of notable chromic shifts between solution and aggregated states, and the pump-probe data collectively indicate that DSAI aggregates operate through localized singlet and triplet excited states.

We then investigated the mechanism underlying this aggregation-induced ROS production. Using TMB oxidation as a read-out, we evaluated the role of molecular oxygen. The oxidation rate was highest under pure O₂ atmosphere, decreased under air, and was nearly abolished under N₂, confirming that the photocatalytic process requires oxygen and light (Fig. 4a and Supplementary Figs. 76 and 77). Scavenger experiments^{51,52} showed that Tiron (3,5-pyrocatecholdisulfonic acid), a superoxide-specific scavenger, considerably suppresses TMB oxidation, whereas D-mannitol (hydroxyl radical scavenger) and L-tryptophan (singlet oxygen quencher) have negligible effect (Fig. 4b and Supplementary Fig. 78). These results point to superoxide (O₂⁻) as the primary intermediate generated by the photoexcited DSAI²⁺ aggregates. Direct detection of O₂⁻ by spin-trapping electron paramagnetic resonance (EPR) spectroscopy with 5,5-dimethyl-1-pyrroline

N-oxide (DMPO) showed the characteristic DMPO–O₂⁻ adduct upon irradiation⁵⁴ (Fig. 4c and Supplementary Fig. 79). In addition, singlet oxygen emission and anthracene-9,10-dipropionic acid photodegradation experiments ruled out singlet oxygen sensitization (Supplementary Fig. 80). Both singlet and triplet excited states of aggregates are involved in electron transfer to O₂ and superoxide formation, as shown by fluorescence quenching (Supplementary Fig. 81) and quenching of the triplet state by ns-TAS (Supplementary Fig. 73).

In the absence of TMB probe or ROS scavengers, photo-generated O₂⁻ can undergo disproportionation or a further one-electron reduction to yield hydrogen peroxide (H₂O₂)^{55,56}. We therefore monitored the production of hydrogen peroxide (H₂O₂) under continuous illumination. H₂O₂ production was linear over time, reaching 2,900 $\mu\text{mol g}^{-1}$ after 4 h (Fig. 4d and Supplementary Fig. 82). Sustained activity requires a sacrificial electron donor, here the buffer 3-(*N*-morpholino)propane-sulfonic acid (MOPS), which reduces the oxidized chromophore (DSA³⁺) and regenerates its ground state, thereby closing the photocatalytic cycle (Supplementary Figs. 83 and 84). Control experiments confirm these requirements: removing DSA aggregates, light, oxygen or the sacrificial donor resulted in no or negligible H₂O₂ production (Fig. 4e). On the basis of these results, we propose that photoexcited DSA aggregates (DSA^{2+*}) transfer an electron to O₂ to form O₂⁻, which undergoes disproportionation or a second one-electron reduction to yield H₂O₂, while the oxidized DSA³⁺ is reduced by a sacrificial donor, to regenerate the ground state and complete the photocatalytic cycle (Fig. 4f). Crucially, aggregation enables this reactivity by stabilizing the excited states and suppressing non-radiative decay through dye rigidification.

The ability to generate superoxide and H₂O₂ under ambient conditions, without metal co-catalysts, highlights the potential of AIP-based supramolecular systems for sustainable photocatalysis. We also demonstrated this by using DSA²⁺ in light-driven oxidation of organic substrates such as 4-(methylthio)phenol to the corresponding sulfoxide in the presence of oxygen (Supplementary Fig. 85). We also investigated the oxidation of glycerol, an abundant feedstock that can be upgraded to value-added chemicals⁵⁷, and found that DSA²⁺ aggregates (DSAI 0.1 mM, NaI 25 mM) exhibit excellent activity for its selective conversion to glyceraldehyde under white-light irradiation (Supplementary Fig. 86).

Aggregation enhances photocatalytic hydrogen evolution

The aggregates show promising electron transfer properties for photocatalysis, as also supported by their calculated excited-state oxidation and reduction potentials relative to commonly used photocatalysts (Supplementary Figs. 87 and 88). The reduction potential of DSA²⁺ is nearly unchanged from the molecular to the aggregate state ($E_{\text{red}} = -1.01 \text{ V}$ versus -1.09 V versus NHE, respectively), as evidenced by electrochemical measurements (Supplementary Fig. 89) and calculations (Supplementary Figs. 90–92). This could be an advantageous feature, because strong hydrophobic interactions and molecular orbitals mixing between monomers often lead to large changes in redox potentials⁵⁸. Thus, preserving redox and excited-state potentials across monomer and aggregate states simplifies predictive design. To assess whether AIP extends beyond oxygen photoreduction, we investigated the ability of DSA²⁺ aggregates to drive hydrogen evolution (Fig. 5a). We first explored photoinduced electron transfer to methyl viologen (MV²⁺), a well-established redox probe ($E^{\circ} = -0.45 \text{ V}$ versus NHE)⁵⁹. Upon irradiation of DSA aggregates we observed an increase in the UV-visible absorption bands of the MV^{•+} radical cation (Fig. 5b), whose formation was confirmed by its characteristic EPR spectrum (Fig. 5c). The ability of the DSA²⁺ to photoreduce MV²⁺ implies that the aggregates could also drive proton reduction ($E^{\circ} = -0.35 \text{ V}$ versus NHE at pH 6).

We then investigated light-driven hydrogen evolution in presence of Pt nanoparticles (PtNPs, pre-made 3-nm colloidal dispersion) as co-catalysts and ascorbic acid (AA) as sacrificial electron donor (Fig. 5a). Interestingly, adding the DSAI to an AA solution dissolved the

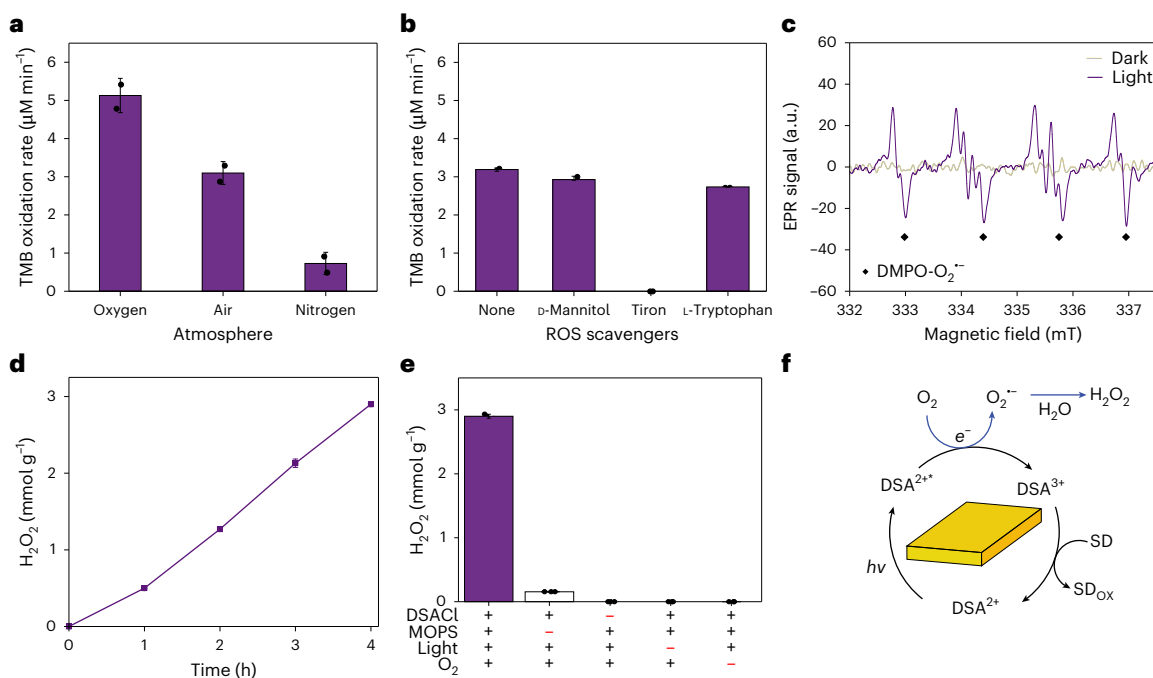


Fig. 4 | Mechanistic insights into ROS generation by irradiation of DSA^{2+} nanostructures. a, Light-driven oxidation rate (5.1 ± 0.4 , 3.1 ± 0.3 and $0.73 \pm 0.29 \mu\text{M min}^{-1}$) of TMB probe ($134 \mu\text{M}$) by DSAI nanostructures (DSAI 0.3 mM) with white light (LED, 180 mW cm^{-2}) under different atmospheres (O_2 , air or N_2). Statistics are from two independent groups. **b**, Light-driven oxidation rate (3.2 ± 0 , 2.9 ± 0.1 , 0.0 ± 0 and $2.8 \pm 0 \mu\text{M min}^{-1}$) of TMB probe ($134 \mu\text{M}$) by DSAI nanostructures (DSAI 0.3 mM) with white light (LED, 180 mW cm^{-2}) in presence of ROS scavengers. Statistics are from two independent groups. **c**, In situ EPR spectra for DSAI nanostructures (DSAI 0.5 mM) and DMPO trap in EDTA (0.1 M ,

pH 6) under dark and irradiation conditions. **d**, H_2O_2 light-driven production over time by irradiation of DSACL nanostructures (DSACL 0.5 mM , NaCl 0.9 M) in MOPS (0.1 M , pH 7.0) with 415 nm (LED, 140 mW cm^{-2}). Statistics are from three independent groups. **e**, Control experiments for H_2O_2 produced by DSACL aggregates (2.9 ± 0 , 0.15 ± 0 , 0.0 ± 0 , 0.0 ± 0 and $0.0 \pm 0 \text{ mmol g}^{-1}$). Statistics are from three independent groups. **f**, Proposed photocatalytic mechanism for H_2O_2 production by the DSA^{2+} nanostructures (SD is the sacrificial donor, specifically MOPS in this case).

powder, probably because DSA^{2+} becomes solubilized through counterion exchange with solvated ascorbate anions. This enabled direct comparison of hydrogen evolution in the molecularly dissolved and aggregated states, the latter obtained by adding NaI under otherwise identical conditions. In the absence of NaI, when DSA^{2+} is dissolved, no H_2 evolution is observed (Fig. 5d and Supplementary Fig. 93). By contrast, NaI-induced charge screening and aggregation increased hydrogen production to over $10,900 \mu\text{mol g}^{-1}$ after 4 h of white-light irradiation (Fig. 5d). Control experiments confirmed that all components (DSAI, AA, PtNPs and light) are essential for the observed activity (Fig. 5e and Supplementary Figs. 94–97). The apparent quantum yield for photocatalytic H_2 evolution was 0.2%, with the photocatalytic activity matching the absorption profile of the aggregate (Supplementary Fig. 98), consistent with reported values for nanostructured chromophore amphiphiles²⁵. Further gains in efficiency could probably be achieved by improving electron-transfer kinetics and interfacial coupling between the aggregates and co-catalysts; for example, in situ photodeposition of PtNPs can promote more efficient electron transfer and a better co-catalyst distribution than impregnation with pre-formed, ligand-capped PtNPs⁴.

After photocatalysis, the supramolecular aggregates were recovered by filtration. The recovered solid remained active, whereas the filtrate showed no activity under identical conditions (Supplementary Figs. 99 and 100), confirming that the photocatalytic function resides in the aggregated state. Consistent with this, aggregated DSAI was also more photostable than the solution species under prolonged illumination, which underwent steady photobleaching (Fig. 5f and Supplementary Fig. 101). Aggregation therefore both enables photocatalysis and stabilizes the chromophore against non-radiative decay and degradation.

Fluorescence experiments revealed that salt-induced aggregation markedly increased emission, with Φ_{Fl} going from 0.8% to 14% (Fig. 5g and Supplementary Fig. 102 for excitation–emission maps), whereas ns-TAS showed the emergence of a triplet state in the aggregated material (Fig. 5h). To quantitatively determine which excited state (singlet or triplet) dominates the productive electron-transfer step under catalytic conditions, we performed quenching experiments (Fig. 5h,i and Supplementary Fig. 103). These experiments revealed that both the excited states of the aggregated DSAI are quenched with increasing concentration of the acceptor MV^{2+} , with the singlet ($k_{\text{sv}}^{\text{S}} = 222 \text{ M}^{-1}$ from fluorescence titration) prevailing over the triplet state ($k_{\text{sv}}^{\text{T}} = 32 \text{ M}^{-1}$ from ns-TAS titration). Altogether, these results show that aggregation enhances not only oxygen reduction but also proton reduction. Both reactivities arise from a common mechanism in which photoexcited DSA^{2+*} aggregates undergo electron transfer to an external acceptor, either molecular oxygen or PtNPs. The higher fluorescence quantum yield of the aggregate indicates a greater abundance of excited states, increasing the probability of productive electron transfer either through singlet- or triplet-state reactivity. Aggregation also confers marked photostability, as shown by suppressed photobleaching under continuous irradiation. These features (higher excited-state utilization, enhanced reactivity and improved stability) further define the scope and advantage of the AIP approach.

Photocatalytic performance depends on aggregation pathway
The DSA nanostructures described so far were obtained immediately upon sample preparation in water (or buffer) and are therefore considered kinetic aggregates. Supramolecular systems, however, often exhibit multiple assembly pathways, and structures formed under kinetic or thermodynamic control can differ markedly in

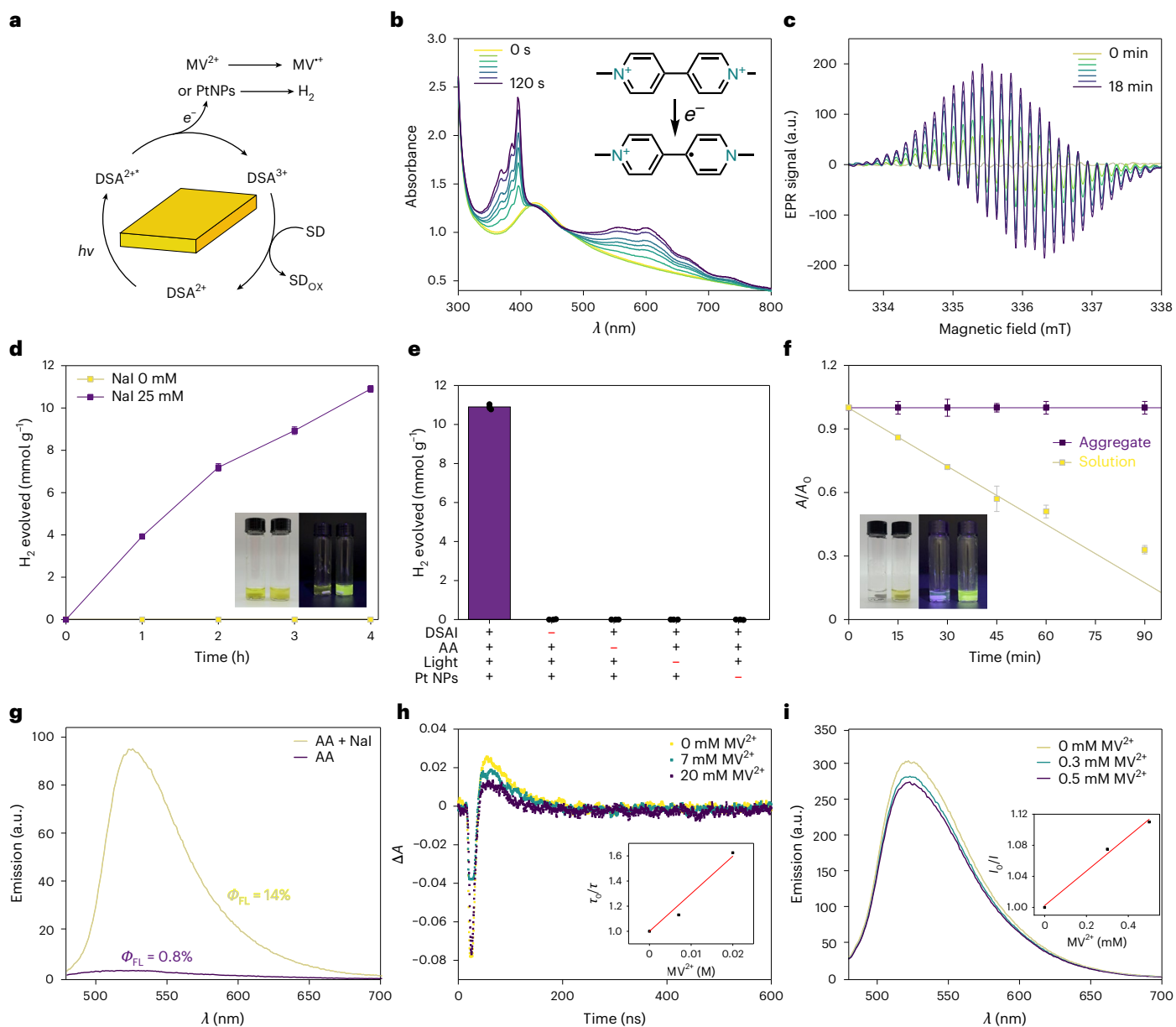


Fig. 5 | Light-driven hydrogen evolution by DSAI²⁺ nanostructures. **a**, Proposed photocatalytic mechanism for methyl viologen (MV²⁺) reduction or hydrogen evolution in presence of a co-catalyst (PtNPs) and sacrificial donor (AA). **b**, UV-visible absorption spectra over time of a mixture of DSAI (1.0 mM) and MV²⁺ (10 mM) under 450 nm (LED, 700 mW cm⁻²) irradiation. **c**, EPR spectra over time of a mixture of DSAI (1.0 mM) and MV²⁺ (10 mM) under 450 nm (LED, 700 mW cm⁻²) irradiation. **d**, H₂ light-driven evolution over time by irradiation of DSAI solution (yellow trace) or nanostructures (NaI 25 mM, purple trace) in AA (1.0 M, pH 4.0), in presence of PtNPs (8% mol) with white light (LED, 100 mW cm⁻²). The inset shows DSAI samples in AA without (left) and with (right) NaI under daylight and UV light. Statistics are from three independent groups. **e**, Control experiments for H₂ produced by DSAI (10.9 ± 0.1, 0.00 ± 0, 0.00 ± 0, 0.00 ± 0 and 0.00 ± 0 mmol g⁻¹). Statistics are from three independent groups.

f, Absorbance over time by irradiation of DSAI solution or DSAI nanostructures in AA. The inset shows irradiated DSAI samples in AA without (left) and with (right) NaI under daylight and UV light. Statistics are from two independent groups. **g**, Emission spectra of DSAI 0.1 mM dissolved in AA 1.0 M (pH 4.0) and aggregated in AA 1.0 M (pH 4.0) with NaI 25 mM ($\lambda_{\text{exc}} = 395$ nm, at isoabsorbance). **h**, Transient absorption kinetic traces at 420 nm of an aqueous solution of aggregates of DSAI 0.05 mM and 2 mM of NaI (yellow trace) and after addition of methyl viologen ([MV²⁺] = 7 mM (green trace) and 20 mM (purple trace). $\lambda_{\text{exc}} = 355$ nm. $A_{355\text{nm}} = 0.31$, 1 cm optical path, 4.4 mJ per pulse. The inset shows the Stern-Volmer analysis. **i**, DSAI 0.1 mM with NaI 0.1 M emission quenching with different MV²⁺ concentration ($\lambda_{\text{exc}} = 470$ nm at isoabsorbance). The inset shows the Stern-Volmer analysis. SD, sacrificial donor.

packing, photophysical properties and functional output^{2,60}. We therefore investigated how kinetically trapped or thermodynamically controlled aggregates differ in structure, emissive behaviour and photocatalytic function.

To study the assembly pathway of DSAI (total concentration, $c_T = 50$ μM) in NaI solution (5.0 mM), we monitored variable-temperature UV-visible absorption. Upon heating, the spectral

changes indicate solubilization of the supramolecular polymer into monomers, whereas cooling shows transition from monomeric DSAI to its aggregate state (Fig. 6a and Supplementary Fig. 104), which we plotted as degree of aggregation (α_{agg})⁶¹⁻⁶³. The non-sigmoidal cooling transition and thermal hysteresis between the critical temperatures of heating ($T_c = 351$ K) and cooling ($T_c' = 306$ K) indicate a nucleation-elongation process⁶¹⁻⁶³. This is further supported by

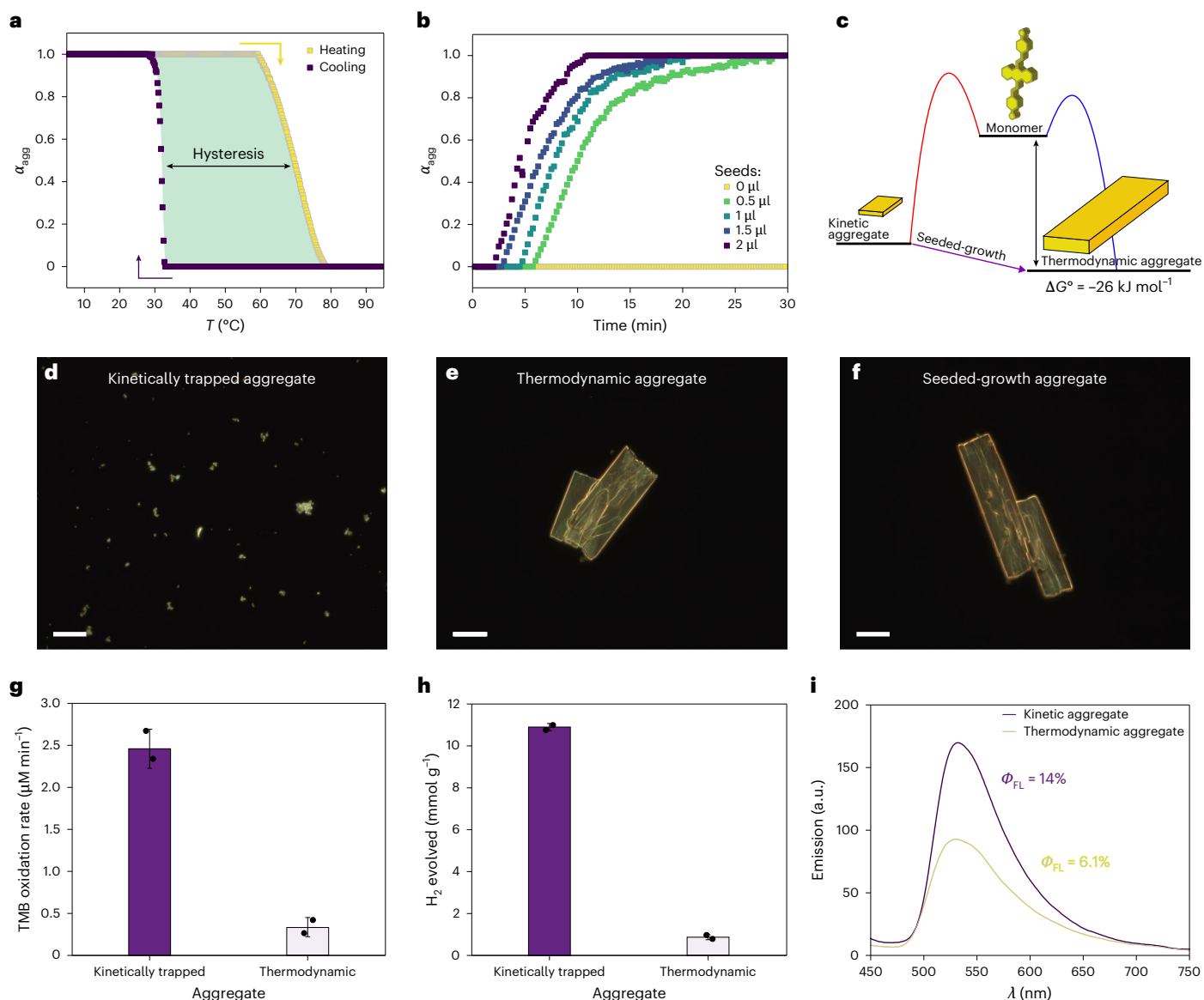


Fig. 6 | Supramolecular polymerization pathways and photocatalysis obtained with DSAI aggregates. **a**, Temperature-dependent degree of aggregation (α_{agg} , estimated from the absorption at 410 nm) of DSAI (c_T 50 μM , NaI 5.0 mM) as a function of temperature upon heating (yellow traces) and cooling (purple traces) at a rate of 1.0 K min^{-1} . **b**, Time-dependent degree of aggregation (α_{agg} , estimated from the absorption at 410 nm) of DSAI (c_T 50 μM , NaI 2.5 mM) upon addition of various amounts of DSAI_{seed} nanostructures (0–2 μl) at 30 °C. **c**, A schematic representation of the free energy landscape in supramolecular self-assembly of DSAI aggregates. **d**, WFM image of kinetically trapped DSAI supramolecular nanostructures in water (DSAI 50 μM , NaI 5.0 mM). Scale bar, 20 μm . **e**, WFM image of thermodynamic DSAI supramolecular

nanostructures in water (DSAI 50 μM , NaI 5.0 mM). Scale bar, 20 μm . **f**, WFM image of seeded-growth DSAI supramolecular nanostructures in water (DSAI 50 μM , NaI 5.0 mM). Scale bar, 20 μm . **g**, TMB oxidation rates (2.5 ± 0.2 , 0.33 ± 0.11 $\mu\text{M min}^{-1}$) by irradiation of various DSAI aggregated states with white light (LED, 180 mW cm^{-2}). Statistics are from two independent groups. **h**, H_2 evolution (10.9 ± 0.2 , 0.87 ± 0.13 mmol g^{-1}) by irradiation of various DSAI aggregated states (0.1 mM) with white light (LED, 100 mW cm^{-2}) in presence of AA (1.0 M, pH 4.0) and co-catalyst (PtNPs, 8% mol). Statistics are from two independent groups. **i**, Fluorescence emission spectra and fluorescence quantum yields (Φ_{FL}) of various DSAI aggregated states.

T_c' shifting to higher temperature as the cooling rate was decreased progressively from 2.0 to 1.0 K min^{-1} (Supplementary Fig. 105). Upon dilution of DSAI, the elongation temperature (T_c') decreased linearly in the van't Hoff plot, from which the standard enthalpy (ΔH°) and entropy (ΔS°) were estimated as -67 kJ mol^{-1} and -139 $\text{J mol}^{-1}\text{K}^{-1}$, respectively (Supplementary Fig. 106). Furthermore, the lag time required to reach the thermodynamic equilibrium enabled supramolecular polymerization and crystal growth to be initiated by seeding. Seeding thermally annealed solutions with increasing amounts of pre-formed nanoribbons at 30 °C accelerated formation of extended crystalline structures and shortened the time to equilibrium (Fig. 6b). A schematic

free energy diagram illustrates the higher energy barrier for direct nucleation than for seeded growth (Fig. 6c), consistent with the lag phase in unseeded samples. Microscopy confirmed that these different pathways lead to distinct morphologies: kinetically trapped aggregates appear as small particles (Fig. 6d and Supplementary Figs. 107–109), whereas seeded and thermodynamic aggregates yield large, well-defined platelets with anisotropic geometries (Fig. 6e,f and Supplementary Figs. 110–115). Strikingly, three-dimensional electron diffraction experiments showed that kinetic and thermodynamic aggregates share the same underlying crystal structure. However, kinetic aggregates display lower diffraction and higher mosaicity

(consistent with faulted stacking, domain boundaries and disorder introduced during rapid, non-equilibrium assembly), whereas thermodynamic aggregates exhibit sharper diffraction indicative of better long-range order (Supplementary Figs. 116–118).

We then compared the photocatalytic performance of thermodynamic and kinetically trapped aggregates, the latter formed under high ionic strength conditions that suppress nucleation-elongation events. ROS generation, measured by TMB oxidation, was notably higher for the kinetically trapped aggregates ($\nu_0 = 2.4 \mu\text{M min}^{-1}$) than for the thermodynamic counterpart ($\nu_0 = 0.33 \mu\text{M min}^{-1}$) (Fig. 6g and Supplementary Fig. 119). Similarly, hydrogen evolution from Pt-catalysed proton photoreduction was higher for the kinetically formed structures (H_2 10,900 $\mu\text{mol g}^{-1}$) than for aggregates obtained upon annealing (H_2 867 $\mu\text{mol g}^{-1}$) (Fig. 6h and Supplementary Fig. 120). Moreover, kinetically trapped aggregates do not grow into their thermodynamic counterparts over several days, as shown by unchanged morphology and comparable photocatalytic activity upon aging (Supplementary Figs. 121 and 122). These functional differences probably originate from the distinct excited-state properties arising from the supramolecular polymerization pathway, as well as differences in surface/volume ratio (Supplementary Fig. 123). Indeed, steady-state fluorescence measurements showed that kinetically formed aggregates possess a higher quantum yield ($\Phi_{\text{FL}} = 14\%$) than thermodynamic aggregates ($\Phi_{\text{FL}} = 6.1\%$, Fig. 6i). This suggests that kinetic aggregation traps chromophores in a state of greater excited-state availability, thereby boosting photoredox efficiency. Taken together, these findings highlight the importance of pathway control in designing functional supramolecular photocatalysts, where transient or metastable states can outperform thermodynamic structures. This contrasts with established crystalline supramolecular polymers, in which the enhanced charge separation in extended nanostructures leads to better H_2 production than in their kinetic counterparts^{2,60}.

Generality of AIP across chromophore scaffolds

To test the generality of AIP, we decided to study an amphiphilic tetraphenylethylene derivative bearing four benzoic acid groups (TBATPE) (Extended Data Fig. 1a). Unlike the DSA²⁺ scaffold, the TBATPE lacks a central π -extended core, but the tetraphenylethylene scaffold is also known to exhibit strong AIE due to restricted intramolecular motion in the aggregate state^{19,64–66}.

TBATPE further supports the generality of AIP. In acidic aqueous media, it forms emissive aggregates (Extended Data Fig. 1b,c and Supplementary Figs. 125 and 126), consistent with aggregation-induced rigidification. These aggregates photocatalyse both TMB oxidation under air ($\nu_0 = 3.8 \mu\text{M min}^{-1}$), with negligible activity in the absence of light or O_2 , and H_2 evolution in the presence of PtNPs and AA, reaching 5,100 $\mu\text{mol g}^{-1}$ after 24 h (Extended Data Fig. 1d,e and Supplementary Figs. 127 and 128). Aggregation is also accompanied by a marked increase in fluorescence quantum yield, from 1.9% in water to 51% in acetate buffer and 60% in AA (Extended Data Fig. 1f), mirroring the trend observed for DSAI. Together, these results show that even a non-planar, nonlinear chromophore such as TBATPE can access fluorescence and photocatalytic activity upon aggregation, despite forming amorphous rather than crystalline assemblies (Supplementary Fig. 129). This supports AIP as a general design principle whereby aggregation-induced rigidification activates otherwise inactive dyes across structurally diverse systems.

Conclusion

We identify AIP as a supramolecular mechanism for organic dyes in water, in which aggregation-induced rigidification suppresses non-radiative decay and stabilizes localized reactive excited states, rather than relying on exciton delocalization or packing-induced changes in electronic structure. In this way, both singlet- and triplet-derived pathways can contribute to photocatalysis⁶⁷, although

singlet reactivity dominates in the present system. Using an amphiphilic distyrylanthracene dye, we show that aggregation controlled by concentration, ionic strength and counterion identity enhances emission, ROS generation and hydrogen evolution from the same molecular scaffold, while leaving the underlying excited-state energetics and redox potentials largely unchanged. The effects of counterion identity and aggregation pathway further show that supramolecular organization can tune function without requiring strong intermolecular electronic coupling. Aggregation-induced rigidification thus complements established covalent rigidification strategies, including sterically constrained structures⁶⁸, covalent organic frameworks, macrocycles, molecular cages and organic–inorganic superlattices^{17,42,69–71}. The observation of the same behaviour in a structurally unrelated tetraphenylethylene-based system, including amorphous aggregates, supports the generality of this concept. More broadly, AIP offers a rich route to molecular photocatalyst design based on localized excited-state reactivity, modular self-assembly and control over aggregation pathway, rather than extended electronic coupling. It thus bridges the defined excited-state reactivity of homogeneous molecular catalysts with the robustness, photostability and recyclability of heterogeneous systems, providing a design paradigm for soft photocatalysts in aqueous media.

Online content

Any methods, additional references, Nature Portfolio reporting summaries, source data, extended data, supplementary information, acknowledgements, peer review information; details of author contributions and competing interests; and statements of data and code availability are available at <https://doi.org/10.1038/s41557-026-02151-4>.

References

- Weingarten, A. S. et al. Self-assembling hydrogel scaffolds for photocatalytic hydrogen production. *Nat. Chem.* **6**, 964–970 (2014).
- Yang, H. et al. Packing-induced selectivity switching in molecular nanoparticle photocatalysts for hydrogen and hydrogen peroxide production. *Nat. Nanotechnol.* **18**, 307–315 (2023).
- Tian, J. et al. Tailored self-assembled photocatalytic nanofibres for visible-light-driven hydrogen production. *Nat. Chem.* **12**, 1150–1156 (2020).
- Zhou, Q., Guo, Y. & Zhu, Y. Photocatalytic sacrificial H_2 evolution dominated by micropore-confined exciton transfer in hydrogen-bonded organic frameworks. *Nat. Catal.* **6**, 574–584 (2023).
- Yu, J. et al. Artificial spherical chromatophore nanomicelles for selective CO_2 reduction in water. *Nat. Catal.* **6**, 464–475 (2023).
- Romero, N. A. & Nicewicz, D. A. Organic photoredox catalysis. *Chem. Rev.* **116**, 10075–10166 (2016).
- Twilton, J. et al. The merger of transition metal and photocatalysis. *Nat. Rev. Chem.* **1**, 0052 (2017).
- Crisenza, G. E. M. & Melchiorre, P. Chemistry glows green with photoredox catalysis. *Nat. Commun.* **11**, 803 (2020).
- Di Terlizzi, L., Nicchio, L., Protti, S. & Fagnoni, M. Visible photons as ideal reagents for the activation of coloured organic compounds. *Chem. Soc. Rev.* **53**, 4926–4975 (2024).
- Guo, Y., Zhou, Q., Zhu, B., Tang, C. Y. & Zhu, Y. Advances in organic semiconductors for photocatalytic hydrogen evolution reaction. *EES Catal.* **1**, 333–352 (2023).
- Wang, L. & Zhu, W. Organic donor–acceptor systems for photocatalysis. *Adv. Sci.* **11**, 2307227 (2024).
- Jing, L., Li, P., Li, Z., Ma, D. & Hu, J. Influence of π – π interactions on organic photocatalytic materials and their performance. *Chem. Soc. Rev.* **54**, 2054–2090 (2025).
- Yu, X. et al. Functional groups-regulated organic semiconductors for efficient artificial photosynthesis of hydrogen peroxide. *Adv. Mater.* **37**, 2501494 (2025).

14. Ashoka, A. H., Aparin, I. O., Reisch, A. & Klymchenko, A. S. Brightness of fluorescent organic nanomaterials. *Chem. Soc. Rev.* **52**, 4525–4548 (2023).
15. Stenspil, S. G. & Laursen, B. W. Photophysics of fluorescent nanoparticles based on organic dyes – challenges and design principles. *Chem. Sci.* **15**, 8625–8638 (2024).
16. Mu, C. et al. Isorecticular preparation of tetraphenylethylene-based multicomponent metallacages towards light-driven hydrogen production. *Angew. Chem. Int. Ed.* **62**, e202311137 (2023).
17. Yang, J.-C. et al. Novel supramolecular artificial light-harvesting systems based on AIE-active macrocycles for efficient white-light photocatalysis in water. *Chem. Sci.* **16**, 4741–4748 (2025).
18. Liu, X. et al. Efficient quasi-homogenous photocatalysis enabled by molecular nanophotocatalysts with donor–acceptor motif. *Adv. Mater.* **37**, 2413440 (2025).
19. Li, W. et al. Artificial light-harvesting systems based on AIEgen-branched rotaxane dendrimers for efficient photocatalysis. *Angew. Chem. Int. Ed.* **60**, 18761–18768 (2021).
20. Gao, Z. et al. Precise supramolecular nanoarchitectonics for simultaneous enhanced photoluminescence and photocatalysis in a co-assembly by a biomimetic isolation-conduction strategy. *Angew. Chem. Int. Ed.* **64**, e202423174 (2025).
21. Samperi, M., Limón, D., Amabilino, D. B. & Pérez-García, L. Enhancing singlet oxygen generation by self-assembly of a porphyrin entrapped in supramolecular fibers. *Cell Rep. Phys. Sci.* **1**, 100030 (2020).
22. Xiong, C. et al. Stabilizing the excited states of organic phosphorescent photosensitizers via self-assembly for CO₂ photoreduction. *Nat. Commun.* **16**, 6140 (2025).
23. Benson, C. R. et al. Plug-and-play optical materials from fluorescent dyes and macrocycles. *Chem* **6**, 1978–1997 (2020).
24. Dumele, O., Chen, J., Passarelli, J. V. & Stupp, S. I. Supramolecular energy materials. *Adv. Mater.* **32**, 1907247 (2020).
25. Cappelletti, D., Barbieri, M., Aliprandi, A., Maggini, M. & Đorđević, L. Self-assembled π -conjugated chromophores: preparation of one- and two-dimensional nanostructures and their use in photocatalysis. *Nanoscale* **16**, 9153–9168 (2024).
26. Shigemitsu, H. et al. Aggregation-induced photocatalytic activity and efficient photocatalytic hydrogen evolution of amphiphilic rhodamines in water. *Chem. Sci.* **11**, 11843–11848 (2020).
27. Bodedla, G. B., Imran, M., Zhao, J., Zhu, X. & Wong, W. Design of AIEgen-based porphyrin for efficient heterogeneous photocatalytic hydrogen evolution: special collection: aggregation-induced processes and functions. *Aggregate* **4**, e364 (2023).
28. McDowall, D. et al. Controlling photocatalytic activity by self-assembly–tuning perylene bisimide photocatalysts for the hydrogen evolution reaction. *Adv. Energy Mater.* **10**, 2002469 (2020).
29. Mao, J. et al. Ultrasmall organic nanocrystal photocatalyst realizing highly efficient symmetry breaking charge separation and transport. *J. Am. Chem. Soc.* **147**, 12730–12739 (2025).
30. Đorđević, L. et al. Mechanical and light activation of materials for chemical production. *Adv. Mater.* **37**, 2418137 (2025).
31. Barbieri, M. et al. Controlled aggregation of pyrene-based supramolecular nanostructures for light-driven switchable H₂ or H₂O₂ production. *Adv. Funct. Mater.* <https://doi.org/10.1002/adfm.202505835> (2025).
32. Aida, T., Meijer, E. W. & Stupp, S. I. Functional supramolecular polymers. *Science* **335**, 813–817 (2012).
33. De Greef, T. F. A. & Meijer, E. W. Supramolecular polymers. *Nature* **453**, 171–173 (2008).
34. Hoeben, F. J. M., Jonkheijm, P., Meijer, E. W. & Schenning, A. P. H. J. About supramolecular assemblies of π -conjugated systems. *Chem. Rev.* **105**, 1491–1546 (2005).
35. Cai, B. et al. Organic crystalline nanoparticles with a long-lived charge-separated state for efficient photocatalytic hydrogen production. *Nat. Chem.* **18**, 723–730 (2026).
36. Hong, Y., Lam, J. W. Y. & Tang, B. Z. Aggregation-induced emission. *Chem. Soc. Rev.* **40**, 5361 (2011).
37. Mei, J., Leung, N. L. C., Kwok, R. T. K., Lam, J. W. Y. & Tang, B. Z. Aggregation-induced emission: together we shine, united we soar! *Chem. Rev.* **115**, 11718–11940 (2015).
38. Würthner, F. Aggregation-induced emission (AIE): a historical perspective. *Angew. Chem. Int. Ed.* **59**, 14192–14196 (2020).
39. Yang, L.-L. et al. Understanding the AIE phenomenon of nonconjugated rhodamine derivatives via aggregation-induced molecular conformation change. *Nat. Commun.* **15**, 999 (2024).
40. Xu, C. et al. Molecular motion and nonradiative decay: towards efficient photothermal and photoacoustic systems. *Angew. Chem. Int. Ed.* **61**, e202204604 (2022).
41. Li, Q. et al. A combination of covalent and noncovalent restricted-intramolecular-rotation strategy for supramolecular AIE-type photosensitizer toward photodynamic therapy. *Aggregate* **6**, e676 (2025).
42. Guo, C.-S. et al. Tetraphenylethylene tricycle-based sequential light-harvesting system through efficient Förster resonance energy transfer for visible light photocatalysis. *Sci. China Chem.* **69**, 245–252 (2026).
43. Zhou, K. et al. Photocatalytic therapy via photoinduced redox imbalance in biological system. *Nat. Commun.* **15**, 10551 (2024).
44. Mei, J. et al. Aggregation-induced emission: the whole is more brilliant than the parts. *Adv. Mater.* **26**, 5429–5479 (2014).
45. Liu, L., Xu, B. & Tian, W. in *Handbook of Aggregation-Induced Emission* (eds Tang, Y. & Tang, B. Z.) 23–52 <https://doi.org/10.1002/9781119643098.ch22> (Wiley, 2022).
46. Du, H. et al. Mapping in situ the assembly and dynamics in aqueous supramolecular polymers. *Nat. Commun.* **16**, 4837 (2025).
47. Gregory, K. P. et al. Understanding specific ion effects and the Hofmeister series. *Phys. Chem. Chem. Phys.* **24**, 12682–12718 (2022).
48. Pappas, C. G. et al. Dynamic peptide libraries for the discovery of supramolecular nanomaterials. *Nat. Nanotechnol.* **11**, 960–967 (2016).
49. Ito, S. et al. Structure determination of small molecule compounds by an electron diffractometer for 3D ED/MicroED. *CrystEngComm* **23**, 8622–8630 (2021).
50. Truong, K.-N. et al. Making the most of 3D electron diffraction: best practices to handle a new tool. *Symmetry* **15**, 1555 (2023).
51. Long, R. et al. Surface facet of palladium nanocrystals: a key parameter to the activation of molecular oxygen for organic catalysis and cancer treatment. *J. Am. Chem. Soc.* **135**, 3200–3207 (2013).
52. Jiao, Y. et al. A Donor–acceptor [2]catenane for visible light photocatalysis. *J. Am. Chem. Soc.* **143**, 8000–8010 (2021).
53. Zhang, J. et al. Insights into the origin of aggregation enhanced emission of 9,10-distyrylanthracene derivatives. *Mater. Chem. Front.* **1**, 1422–1429 (2017).
54. Clément, J.-L. et al. Assignment of the EPR spectrum of 5,5-dimethyl-1-pyrroline N-oxide (DMPO) superoxide spin adduct. *J. Org. Chem.* **70**, 1198–1203 (2005).
55. Sawyer, D. T. & Valentine, J. S. How super is superoxide?. *Acc. Chem. Res.* **14**, 393–400 (1981).
56. Bielski, B. H. J., Cabelli, D. E., Arudi, R. L. & Ross, A. B. Reactivity of HO₂/O₂⁻ radicals in aqueous solution. *J. Phys. Chem. Ref. Data* **14**, 1041–1100 (1985).
57. Tacchi, E., Rossi, G., Natali, M., Đorđević, L. & Sartorel, A. Aqueous photocatalytic glycerol oxidation to formic acid coupled to H₂O₂ production with an anthraquinone dye. *Adv. Sustain. Syst.* **9**, 2400538 (2025).

58. Ashcraft, A. et al. A molecular strategy to lock-in the conformation of a perylene bisimide-derived supramolecular polymer. *Angew. Chem. Int. Ed.* **59**, 7487–7493 (2020).
59. Bird, C. L. & Kuhn, A. T. Electrochemistry of the viologens. *Chem. Soc. Rev.* **10**, 49 (1981).
60. Kazantsev, R. V. et al. Crystal-phase transitions and photocatalysis in supramolecular scaffolds. *J. Am. Chem. Soc.* **139**, 6120–6127 (2017).
61. Jonkheijm, P., Van Der Schoot, P., Schenning, A. P. H. J. & Meijer, E. W. Probing the solvent-assisted nucleation pathway in chemical self-assembly. *Science* **313**, 80–83 (2006).
62. Ogi, S., Stepanenko, V., Sugiyasu, K., Takeuchi, M. & Würthner, F. Mechanism of self-assembly process and seeded supramolecular polymerization of perylene bisimide organogelator. *J. Am. Chem. Soc.* **137**, 3300–3307 (2015).
63. Wehner, M. & Würthner, F. Supramolecular polymerization through kinetic pathway control and living chain growth. *Nat. Rev. Chem.* **4**, 38–53 (2019).
64. Zhang, Q., Dang, X., Cui, F. & Xiao, T. Supramolecular light-harvesting systems utilizing tetraphenylethylene chromophores as antennas. *Chem. Commun.* **60**, 10064–10079 (2024).
65. Sun, H. et al. Charge separation to facilitate the conversion of copper-phenylacetylide from aggregation-induced emission to efficient photocatalysis. *Adv. Funct. Mater.* **34**, 2311591 (2024).
66. Wang, F.-D. et al. Tetraphenylethylene-based photoresponsive supramolecular organic framework and its metallization for photocatalytic redox reactions. *J. Mater. Chem. A* **12**, 16190–16199 (2024).
67. Liu, R. et al. Harvesting singlet and triplet excitation energies in covalent organic frameworks for highly efficient photocatalysis. *Nat. Mater.* **24**, 1245–1257 (2025).
68. Gao, F. et al. In-solution intramolecular through-space conjugations of sterically constrained tetranaphthylethane. *CCS Chem.* **8**, 234–245 (2026).
69. Ding, H. et al. An AI-Egen-based 3D covalent organic framework for white light-emitting diodes. *Nat. Commun.* **9**, 5234 (2018).
70. Qin, Y. et al. Construction of covalent organic cages with aggregation-induced emission characteristics from metallacages for mimicking light-harvesting antenna. *Angew. Chem. Int. Ed.* **62**, e202308210 (2023).
71. Wang, K. et al. Two-dimensional-lattice-confined single-molecule-like aggregates. *Nature* **633**, 567–574 (2024).

Publisher's note Springer Nature remains neutral with regard to jurisdictional claims in published maps and institutional affiliations.

Open Access This article is licensed under a Creative Commons Attribution 4.0 International License, which permits use, sharing, adaptation, distribution and reproduction in any medium or format, as long as you give appropriate credit to the original author(s) and the source, provide a link to the Creative Commons licence, and indicate if changes were made. The images or other third party material in this article are included in the article's Creative Commons licence, unless indicated otherwise in a credit line to the material. If material is not included in the article's Creative Commons licence and your intended use is not permitted by statutory regulation or exceeds the permitted use, you will need to obtain permission directly from the copyright holder. To view a copy of this licence, visit <http://creativecommons.org/licenses/by/4.0/>.

© The Author(s) 2026

Methods

Samples preparation

For counterion-dependent studies, DSAX ($X = \text{Cl}^-$, Br^- , NO_3^- , I^- and PF_6^-) stock solutions in dimethyl sulfoxide (DMSO) (30 mM) were diluted into water to give samples at 1.5, 1.0, 0.15, 0.10 and 0.05 mM in DMSO (5% v/v), with stirring before each measurement. For solvent-composition studies, a DSAI suspension in water (3 mM) was diluted with defined DMSO/ H_2O mixtures to obtain samples at 1.5, 1.0, 0.75, 0.50 and 0.25 mM containing 0–40% DMSO (v/v). For ionic-strength studies, aqueous DSAI samples (0.5 mM) were prepared with variable NaI concentration (0–0.5 mM) by dilution of stirred DSAI (1 mM) and NaI (25 mM) stock solutions. The DSAI-NaI samples were then diluted to obtain the final concentrations (DSAI 0–0.3 mM and NaI 0–0.5 mM) and were stirred for 10 min before Φ_{FL} measurements.

Microscopy samples were prepared with DSAX-based aggregates under defined ionic and thermal conditions. DSAI samples were prepared by adding a NaI solution (1 M) to a DSAI solution (0.05 mM) to reach a final concentration of DSAI 0.05 mM and NaI 0.5 mM. For the supramolecular pathways studies, kinetic aggregates (DSAI 0.05 mM, NaI 5 mM) were prepared by adding NaI stock solution (1 M) to a DSAI solution (0.05 mM); thermodynamic aggregates were obtained by heating the same mixture to 95 °C for 2 min followed by slow cooling overnight; for seeded-growth samples, a small aliquot of pre-formed DSAI seeds was added to a DSAI solution at 50 °C during the cooling process, giving a 49:1 ratio of dissolved DSAI to seeds. DSAX samples were prepared from DSACl, DSABr and DSANO₃ at 0.05 mM with the corresponding added salts (NaCl, NaBr or NaNO₃), or NaI for DSACl, followed by 5–15 min stirring. DSAPF₆ samples were prepared either by direct sonication in water or by nanoprecipitation from DMSO (0.1 ml of 5 mM) into water (1.9 ml) under stirring.

Absolute fluorescence quantum yields (Φ_{FL})

Measurements were performed with Quantaaurus-QY Absolute PL quantum yield spectrometer C11347-11 integrating sphere in air-equilibrated condition using an empty quartz tube as a reference. For DSAX samples, 360–480 nm excitation wavelengths (20 nm steps) were used. The final Φ_{FL} represents the average, which was calculated from the quantum yields measured at different excitation wavelengths.

ROS experiments

The photooxidation experiments of TMB were performed in air atmosphere using quartz cuvettes (10 mm path length) with a PTFE lid. A stock sample of DSAX ($X = \text{Cl}^-$, Br^- , NO_3^- or I^-) (0.4 mM) in acetate buffer (0.1 M, pH 5) was sonicated for 10 min and then diluted to 0.3 mM DSAX with acetate buffer (3 ml total volume), followed by addition of 0.1 ml of TMB (1 mg ml⁻¹ in DMSO) under stirring. In the case of DSAPF₆, a stock solution in DMSO (18 mM) was added (0.05 ml) to acetate buffer solution (3 ml) under stirring, followed by addition of TMB (0.05 ml, 2 mg ml⁻¹ in DMSO). All DSAX samples (final concentration of 0.3 mM) were left under stirring at least 1 h at room temperature. For DSAI concentration-dependent studies, the DSAI stock sample (0.4 mM) was diluted with acetate buffer to obtain the final concentration (3 ml of 0.1, 0.2, 0.3 and 0.4 mM), before adding 0.1 ml of TMB (1 mg ml⁻¹ in DMSO) under stirring and stirring for 1 h. For NaI concentration screening, different dilutions of a NaI stock (20 mM) in acetate buffer (0.1 M at pH 5) were prepared (1.5 ml), followed by addition of 1.5 ml of DSAI suspension (0.2 mM in acetate buffer) under stirring to obtain DSAI samples (0.1 mM) with final NaI concentrations of 0, 0.2, 0.4 and 0.6 mM, respectively. Then, 0.1 ml TMB (1 mg ml⁻¹ in DMSO) was added to the vials and left under stirring under equilibration (monitored by UV-visible spectroscopy). TMB final concentration in all samples was 134 μM . Experiments under O₂ and N₂ atmosphere were performed in quartz cuvettes (10 mm path length) with screw cap and sealed with silicone/PTFE septum. Cuvettes were positioned into a homemade built photoreactor using a three-dimensional printed

sample support and white-light light-emitting diodes (LEDs) (irradiation at 180 mW cm⁻²). The TMB oxidation process was monitored with UV-visible spectroscopy by focusing on the absorption band of oxidized TMB ($\epsilon_{652} = 3.9 \times 10^4 \text{ M}^{-1} \text{ cm}^{-1}$).

Photoproduction of hydrogen peroxide

A stock solution of DSACl (0.5 mM) in 3-(*N*-morpholino)propanesulfonic acid (0.1 M, pH 7.0) was prepared. A total of 1.0 ml of this solution was transferred to a 9.0 ml screw cap vial. Then, powdered NaCl (53 mg, 0.90 mmol) was added to prepare the aggregated samples. Vials were then purged for 15 min with O₂ by using steel needles through the septum as inlet (longer needle inside the solution) and outlet (shorter needle in the headspace). Then the purging was stopped, the long needle was retracted to the headspace, and then the short one was removed. The vials were illuminated under stirring at 300 rpm using a homebuilt photoreactor made of 415 nm light LEDs with a light intensity of 140 mW cm⁻². Hydrogen peroxide concentrations were determined using horseradish peroxidase enzyme and TMB method³⁰.

Photocatalytic H₂ evolution

A stock solution of DSAI (0.1 mM) in AA (1 M, pH 4.0) was prepared. Then, 973 μl of this solution was transferred to a 9.0 ml screw cap vial, followed by addition of pre-made PtNPs (1.6 μl ; 3 nm particle size, 1,000 ppm in H₂O, Sigma-Aldrich). Then, 25 μl of a NaI stock solution (1 M) was added to prepare the aggregated samples, whereas 25 μl of H₂O was added to prepare the solution samples. Vials were then purged for 15 min with N₂, followed by equilibration to atmospheric pressure and irradiated with white-light LED (100 mW cm⁻²) under 300 rpm stirring. The produced H₂ was detected using a gas chromatograph (Agilent Technologies 8860 with autosampler PAL3 coupled with TCD detector at 250 °C) by injecting 100 μl from the headspace, and the H₂ evolved was calculated using a calibration plot.

For details of the molecular synthesis and the photophysical, photocatalytic, microscopic and electron diffraction experiments, please refer to the Supplementary Information.

Data availability

All the data supporting the findings of this study are available within the Article and its Supplementary Information and also from the corresponding author upon request. The X-ray crystallographic coordinates for structures reported in this study have been deposited at the Cambridge Crystallographic Data Centre (CCDC), under deposition number CCDC-2485494. These data can be obtained free of charge via The Cambridge Crystallographic Data Centre at www.ccdc.cam.ac.uk/data_request/cif. Source data are provided with this paper.

Acknowledgements

This work was funded by the European Union (ERC, PhotoDark, 101077698) (L.Đ.). Views and opinions expressed are however those of the authors only and do not necessarily reflect those of the European Union or the European Research Council. Neither the European Union nor the granting authority can be held responsible for them. The work carried out in the Arcudi laboratory was funded with the contribution of the Italian Ministry of University and Research under DD no. 1236 of 01/08/2023 – FIS 2 call (ENGCAT, FIS-2023-02956, C53C25000170001) (F.A.). M.B. is grateful for the PhD scholarship funded by the MUR Excellence Department Project C² (awarded to the Department of Chemical Sciences, University of Padova). Lifetime experiments were performed on Edinburgh FLS 1000 UV/Vis/NIR photoluminescence spectrometer, funded by the MUR Excellence Department project Nexus (awarded to the Department of Chemical Sciences, University of Padova). L.C. thanks the University of Modena and Reggio Emilia for financial support. We are grateful to I. Fortunati and A. Basagni (University of Padova) for their help with photoluminescence and microscopy experiments, respectively.

Author contributions

M.B., D.C. and L.V. performed most of the experiments, including synthesis, characterization and photocatalysis. L.C., K.-N.T. and F.N. carried out the single-crystal structure determination. M.V. and P.C. performed the transient absorption spectroscopy experiments and analysed the data. E.P., A.A. and F.A. contributed to the photophysical characterization. A.S. performed the electrochemical measurements. L.Đ. conceived and directed the research, performed part of the experimental work and wrote the manuscript. All authors contributed to revising the manuscript and approved the final version.

Funding

Open access funding provided by Università degli Studi di Padova within the CRUI-CARE Agreement.

Competing interests

The authors declare no competing interests.

Additional information

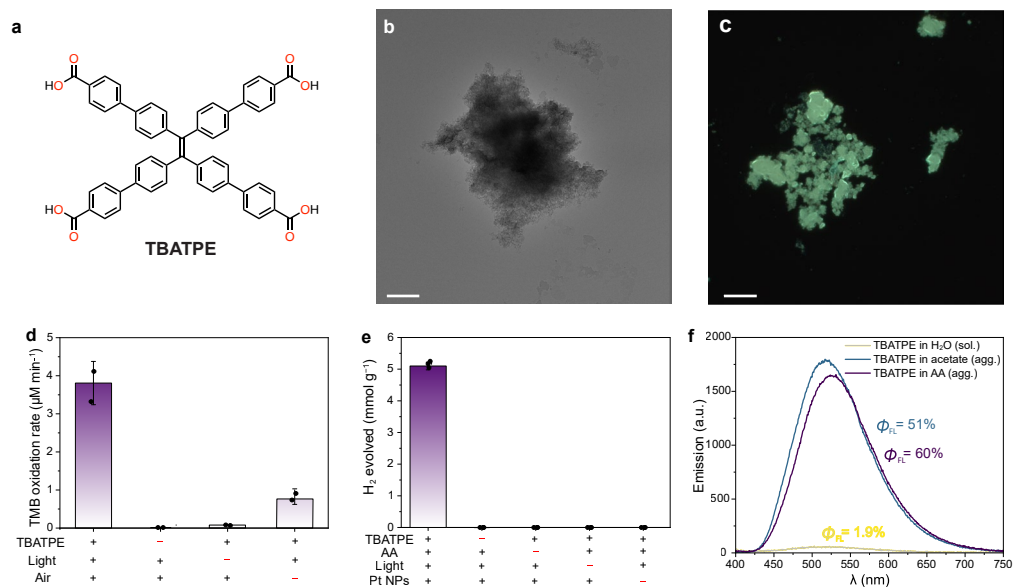
Extended data is available for this paper at <https://doi.org/10.1038/s41557-026-02151-4>.

Supplementary information The online version contains supplementary material available at <https://doi.org/10.1038/s41557-026-02151-4>.

Correspondence and requests for materials should be addressed to Luka Đorđević.

Peer review information *Nature Chemistry* thanks George Pistolis and the other, anonymous, reviewer(s) for their contribution to the peer review of this work. Peer reviewer reports are available.

Reprints and permissions information is available at www.nature.com/reprints.



Extended Data Fig. 1 | Generalizing aggregation-induced photocatalysis with a tetraphenylethylene derivative (TBATPE). **a**, Chemical structure of TBATPE derivative. **b**, Transmission electron microscope (TEM) image of TBATPE aggregates in AA (TBATPE 0.1 mM, AA 5 mM). Scale bar is 1 μm . **c**, Widefield fluorescence microscope (WFM) image of TBATPE supramolecular aggregates in AA (TBATPE 0.1 mM, AA 5 mM). Scale bar is 20 μm . **d**, TMB oxidation rates and controls (3.8 ± 0.6 , 0.0 ± 0 , 0.08 ± 0.01 , $0.82 \pm 0.12 \mu\text{M min}^{-1}$) by irradiation of TBATPE aggregates (0.2 mM) with white light (LED, 180 mW cm^{-2}) in presence

of acetate buffer (60 mM, pH = 5). Statistics are from 2 independent groups. **e**, H_2 evolution and controls (5.1 ± 0.1 , 0.0 ± 0 , 0.0 ± 0 , 0.0 ± 0 , $0.0 \pm 0 \text{ mmol g}^{-1}$) by irradiation of TBATPE aggregates (0.1 mM) with 415 nm (LED, 140 mW cm^{-2}) in presence of ascorbic acid (0.8 M, pH = 4.0) and co-catalyst (PtNPs, 8% mol). Statistics are from 3 independent groups. **f**, Fluorescence emission spectra and fluorescence quantum yields (Φ_{PL}) of TBATPE solution and aggregates under the photocatalytic conditions.